Synchrotron Sub-μ X-ray Tomography of Kirkendall Porosity in a Diffusion Couple of Nickel-Base Superalloy and Nickel after Annealing at

ADVANCED ENGINEERING MATERIALS
www.aem-journal.com

Synchrotron Sub-μ X-ray Tomography of Kirkendall Porosity in a Diffusion Couple of Nickel-Base Superalloy and Nickel after Annealing at 1250 °C

Alexander Epishin, Bettina Camin, Lennart Hansen, Anton Chyrkin, and Gert Nolze*

Kirkendall porosity that forms during interdiffusion in a diffusion couple of nickel-base superalloy CMSX-10 with pure nickel is investigated. The diffusion experiments are conducted at a temperature of 1250 °C, where the strengthening γ′-phase is partially dissolved. The porosity is studied by X-ray sub-μ tomography with a spatial resolution of about 0.35^3 μm^3 at the European Synchrotron Radiation Facility (ESRF) in Grenoble, France. It is found that depending on the distance from the interface the Kirkendall pores take different shapes: octahedral, rounded pyramidal, drop shaped, dendritic, pear shaped, and joint shapes. Such a variety of pore morphologies indicates a complex multistage process of porosity nucleation and growth under vacancy supersaturation of different degrees. The experimental findings are interpreted on the basis of the results of diffusion modeling. It is shown that the kinetics of porosity growth is essentially influenced by the dissolution of the γ′-phase.

1. Introduction

Interdiffusion in joints of alloys at elevated temperatures is accompanied by the growth of pores via the absorption of supersaturated vacancies, known as Kirkendall porosity.[1,2] This process results in the damage of joints during operation, which deteriorates their mechanical strength. Therefore, experimental investigation and modeling of the growth of Kirkendall pores is of significant practical interest.[3–8] For example, considerable modeling efforts have been undertaken on the analysis of competition between Kirkendall and Frenkel effects, that is, between the diffusion transfer of atomic planes over the interface, resulting in the interface shift and the formation of pores via the absorption of supersaturated vacancies.[4–7]

Kirkendall porosity is usually examined by optical microscopy, which, due to low spatial resolution and 2D imaging, provides very limited information, e.g., the porosity area fraction and pore size. Such information is not sufficient for the development of new, sophisticated models of porosity evolution and, therefore, it has to be extended and refined. An advanced method to characterize microporosity is high-resolution synchrotron X-ray tomography. Earlier we used this method to investigate microporosity in single-crystal nickel-base superalloys in different conditions (as cast, heat treated, after creep), and these investigations demonstrated the high efficiency of this technique for porosity characterization.[9] In this work, we applied X-ray sub-μ tomography to investigate Kirkendall porosity in a diffusion couple of a single-crystal nickel-base superalloy CMSX-10 with pure nickel previously investigated by other methods. The investigation of interdiffusion in this diffusion couple by electron probe microanalysis (EPMA)[10] and modeling with diffusion simulation software Dictra[11] showed that porosity intensively grows in the CMSX-10 part. This occurs due to the strong afflux of vacancies coming from the Ni part of the diffusion couple to CMSX-10 to compensate the fast efflux of aluminum from CMSX-10 to Ni. Scanning electron microscopy (SEM) indicated that the growing Kirkendall pores have complex shapes which, however, could not be characterized and explained on the base of SEM observations of the sample 2D sections. The present work aims at a comprehensive investigation of this porosity using X-ray sub-μ tomography which enables 3D imaging of pores with a spatial resolution of about 0.35^3 μm^3.

2. Results

Figure 1a shows the combined EMPA and SEM results similar to that obtained in our previous work[10] (unpublished repeated

Dr. A. Epishin, Dr. B. Camin, L. Hansen
Faculty III Process Sciences
Metallic Materials Engineering
Institute for Materials Science and Technology
Technical University of Berlin
Sekr. BH18, Ernst-Reuter-Platz 1, Berlin 10587, Germany
E-mail: a.epishin@tu-belin.de, alex_epishin@yahoo.de

Dr. A. Chyrkin
Division of Energy and Materials
Department of Chemistry and Chemical Engineering
Chalmers University of Technology
Kemivägen 10, 412 96 Gothenburg, Sweden

Dr. G. Nolze
Division Materialography
Fractography and Ageing of Engineered Materials
Department of Materials Engineering
Federal Institute for Materials Research and Testing
Unter den Eichen 87, 12205 Berlin, Germany

The ORCID identification number(s) for the author(s) of this article can be found under https://doi.org/10.1002/adem.202001220.

DOI: 10.1002/adem.202001220

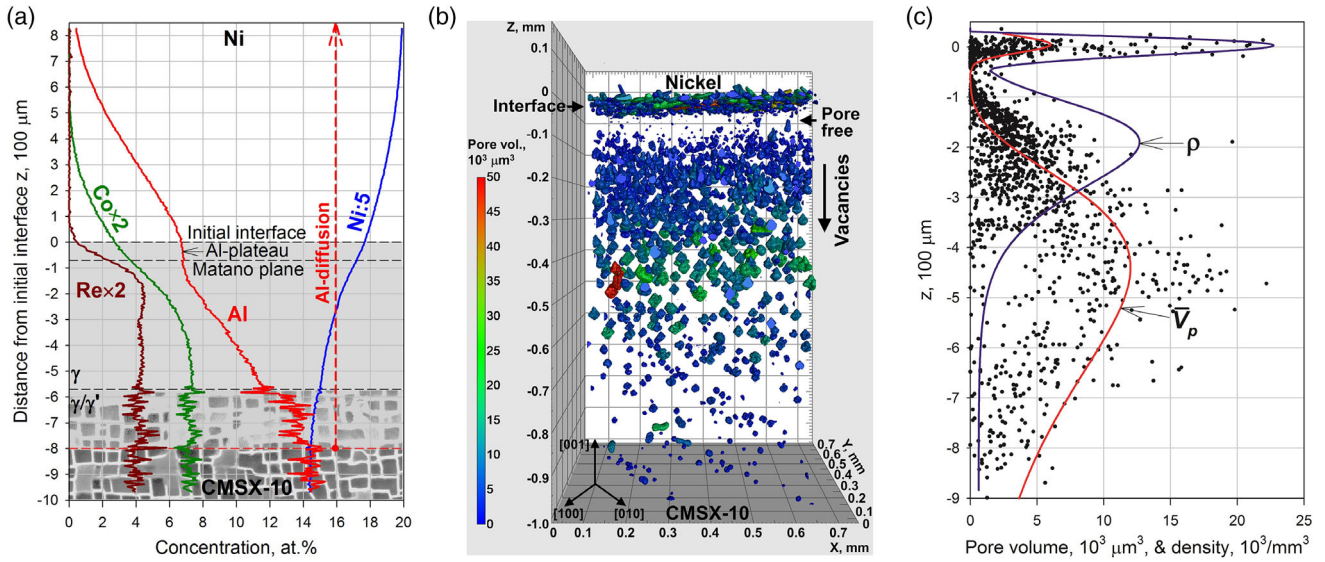

Figure 1. Distribution of elements (a) and porosity (b, c) in the diffusion couple CMSX-10/Ni after 192 h of annealing at 1250 °C. a) Concentration of N in is divided by a factor of 5, Co and Re multiplied by 2. b) Overview of X-ray tomogram. The nickel part is at the top, the CMSX-10 part below it. The color scale indicates the pore volume. c) Changes of the pore volume and density with a distance from the interface. The lines marked with $\bar{V}_p$ and ρ, respectively, show changes of the local values of pore volume and density averaged over the sample cross section. The dots represent the volume of each pore.

measurements). The graph shows the concentration profiles of Ni, Al, Cr, and Re in the diffusion couple CMSX-10/Ni after 192 h of annealing at 1250 °C. The nickel part is at the top, the CMSX-10 part below it. The vertical position of the original interface (weld) is taken as a reference position with $z = 0$. The background schematically shows the microstructure of superalloy CMSX-10 at the end of annealing. It is seen that in the area between $z = 0$ and $z \approx -570$ μm, the γ′ phase is totally dissolved and the alloy has a single-phase γ structure. In the area lying below, between $z \approx -570$ and $z \approx -800$ μm, the γ′ phase dissolves, and the lower border of this area coincides with the end of the Al diffusion zone shown by a red dashed horizontal line. Below $z \approx -800$ μm, the diffusion processes are insignificant and the γ/γ′ microstructure is still stable. A significant finding in the study by Epishin[10] is a plateau in the Al profile enclosed between the original interface and Matano plane located at $z_M \approx -70$ μm. Because z_M determined by processing the concentration profiles of different elements should be exactly the same,[12] it is easier to find it using the narrow symmetric profile of Re. It is shown in Figure 1a that a black dashed horizontal line at $z_M = -70$ μm crosses the Re diffusion zone exactly in the middle.

Figure 1b shows an overview of porosity in a volume of about $0.7 \times 0.7 \times 1.1$ mm^3 of annealed diffusion couple CMSX-10/Ni. The ⟨001⟩ basis vectors refer to the orientation of the CMSX-10 single crystal. The color scale indicates the pore volume. The initial interface at $z = 0$ can be recognized as a plane arrangement of pores grown directly in the weld seam. No pores are visible in the nickel part, whereas the CMSX-10 part contains numerous Kirkendall pores whose density changes with a distance z from the interface. It is remarkable that a short area of about 100 μm in length below the interface is nearly free of pores. Further Kirkendall porosity starts and extends far to the image bottom. This is consistent with the length of the Al diffusion zone in CMSX-10, as shown in Figure 1a.

Figure 1c shows changes of the pore volume $\bar{V}_p$ and density ρ with a distance z from the interface. The lines marked with $\bar{V}_p$ and ρ respectively show changes of the local values of pore volume and density averaged over the sample cross-section. The dots give the volumes of individual pores. The porosity in the interface is characterized by the peak values of $\bar{V}_p$ and ρ, respectively $\bar{V}_p \approx 6 \times 10^3$ μm^3 and $\rho \approx 22.5 \times 10^3$ pore mm^{-3}, and its volume fraction exceeds 10 vol%. In a low-porosity area beneath the interface, the porosity volume fraction is about 0.1 vol%, which is even lower than that in the original CMSX-10 (0.30 vol%). The local values of $\bar{V}_p$ and ρ are correspondingly low with $\bar{V}_p < 500$ μm^3 and $\rho \approx 2 \times 10^3$ pore mm^{-3}. For $z < -100$ μm, $\bar{V}_p$ and ρ change with different rates. The pore volume $\bar{V}_p$ increases over a long distance, reaches a maximum value at $z \approx -450$ μm, slightly exceeding 12×10^3 μm^3, but then decreases. Such a change of $\bar{V}_p$ fits with the color visualization of the pore volume in Figure 1b. The pore density ρ increases much faster, reaching a maximum of 12.5×10^3 pore mm^{-3} at $z \approx -200$ μm, but then monotonically decreases. The average volume fraction of Kirkendall porosity in the area located between $z = -100$ and -800 μm is of about 2.2 vol%, that is, about 7 times higher than that in heat-treated CMSX-10.

Figure 2 shows the evolution of the pore shape in detail. Below the Al diffusion zone at $z < -800$ μm (bottom of Figure 1b), the pores have the original rounded shapes typical for fully heat-treated superalloys. In Figure 2a, two types of original pores can be distinguished: smaller spherical pores of about 15 μm in diameter and larger stretched pores extending up to about 60–70 μm in length. According to the study by Epishin,[13] the first pores are defined as homogenization (H) pores and the second ones as solidification (S) pores. The formation of H and S

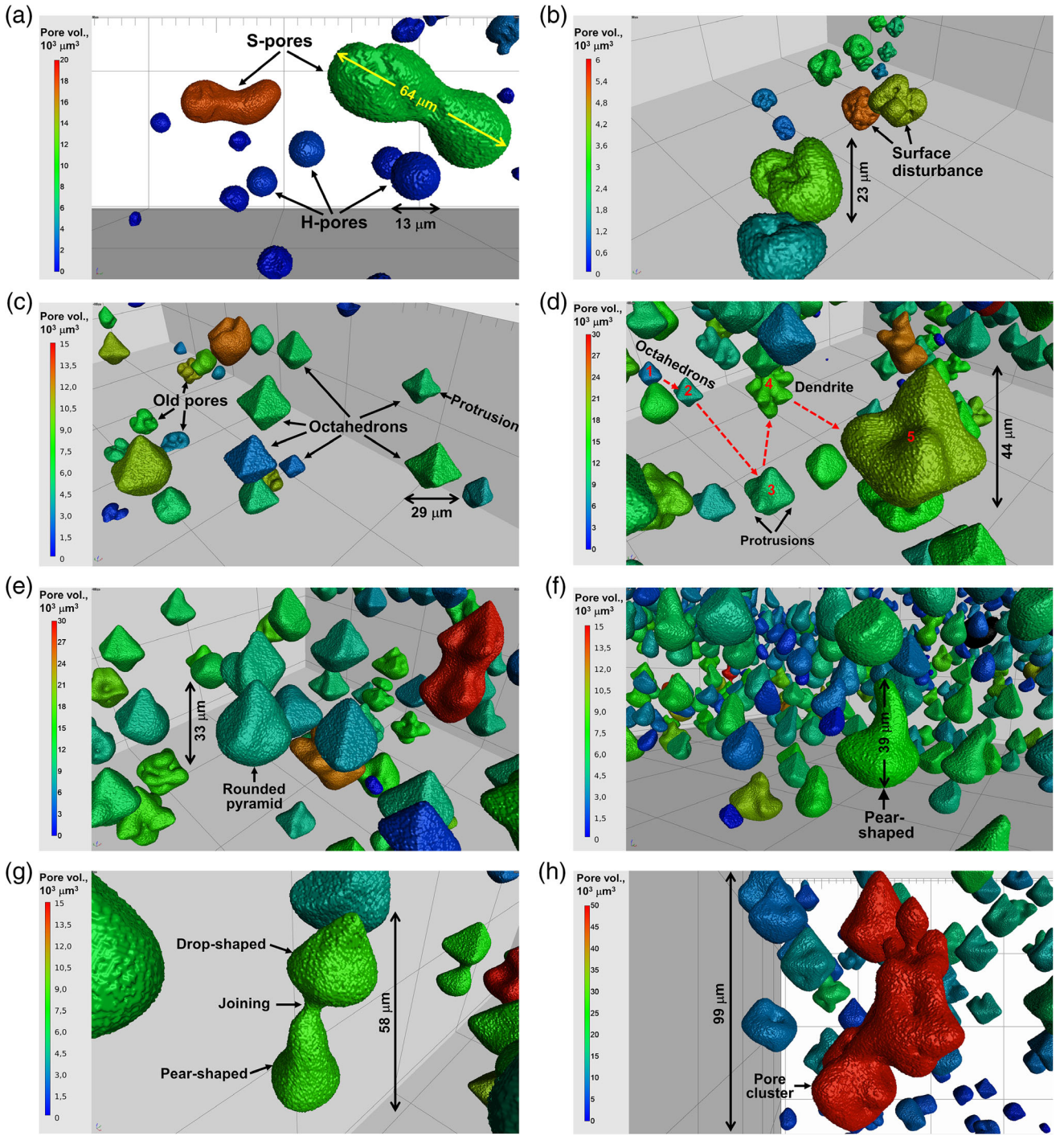

Figure 2. Pores of various morphologies observed in diffusion couple CMSX-10/N at different distances from the interface after 192 h of annealing at 1250 °C. a) Original S and H pores with a rounded surface. b) Original pores with a disturbed surface. c) Old pores of irregular shape and new octahedral pores. d) Transition of octahedral pores, marked as 1, 2, and 3, into pores of dendritic shape and rounded dendritic shapes, marked as 4 and 5, respectively. e, f) Pores above the area of dendritic growth. g) Joining of pear- and drop-shaped pores. h) Joining of several pores into a cluster. The color scales give the pore volume. Double-sided arrows give the linear size of specific individual pores.

pores is discussed in studies,[14,15] respectively. As known from the SEM results of Figure 1a, the γ′ precipitates start to dissolve slowly at the distance from the interface of about 800 µm. This results in Al flux to the interface, which activates a counter-flux of vacancies, as shown schematically by a vertical arrow in Figure 1b. Due to the increasing concentration of vacancies, the pre-existing pores

increase slightly in volume, their surface becomes unstable and takes a wavy shape, as shown in Figure 2b.

At the distance from the interface of about 600 μm in addition to the old pores of irregular shapes, the new crystallographically shaped pores appear, see the small blue pores in Figure 2c. These new pores nucleate as right octahedrons faced by {111} planes, that is, planes with a minimum specific surface energy $\gamma_{(hkl)}$. It is known that for fcc crystals the following relation is valid: $\gamma_{(111)} > \gamma_{(011)} > \gamma_{(001)}$, e.g., see studies.[16,17] Due to their crystallographic shape, such pores are called as "negative crystals."[18] When one looks closely, one can see that during further growth, the octahedral shape slightly changes and small protrusions form in the ⟨001⟩-oriented vertices, see the larger green octahedral pores.

Figure 2d shows the next step of porosity evolution at the distance from the interface of about 500 μm. One should distinguish here the pores of following shapes: pores of the right octahedral shape, e.g., pores numbered as 1 and 2, octahedral pores with clear protrusions in the ⟨001⟩ oriented vertices, e.g., a pore numbered as 3, pores of a pronounced dendritic shape with the ⟨001⟩ oriented arms, e.g., a pore numbered as 4, and a large pore numbered as 4 which looks like a rounded dendrite. The volume of the pores numbered from 1 to 5 increases as 6.0×10^3, 8.8×10^3, 10.8×10^3, 17.1×10^3, and 20.8×10^3 μm^3 and, therefore it is logical to conclude that they correspond to the sequent change of their shape, as shown by dashed arrows in Figure 2d. The growth of ⟨001⟩ protrusions in the octahedron vertices obviously results in the development of ⟨001⟩ dendritic arms. It is remarkable that the dendritic arms are faced by {111} planes, i.e., as well as the octahedral pores. However, when the dendritic growth slows down, the surface of a dendritic pore should straighten and round, leading to a pore shape similar to the pore 5.

Figure 2e–g shows the pores above the area of dendritic growth. It is seen visually from Figure 2f as well as from Figure 1b that the pore density here is significantly increased. This indicates that the growth of already-existing pores is accompanied by the nucleation of new ones. This also follows from the quantified monotonic increase in pore density moving from $z = -700$ μm to $z = -200$ μm, see Figure 1c. The following new shapes of pores can be distinguished here: 1) a rounded square pyramid with the convex base, see Figure 2e; 2) a pear shape, see Figure 2f; and 3) a drop shape, see Figure 2g. A general feature of all these pores is a rounded anisotropic shape with a tip oriented toward the interface where the vacancies come from. A pear-shaped pore in Figure 2f is similar to the pore marked as 5 in Figure 2d. So a pore of such a shape could develop through a step of dendritic growth. However, it is difficult to imagine that a pore of a rounded pyramidal shape (Figure 2e) also results from the dendritic growth. Such a pore shape could be rather a result of the direct transformation of an octahedral pore by rounding the corners between the adjacent pyramidal faces. Further rounding could result into a drop-shaped pore shown in Figure 2g.

The elongation of the pores toward the interface results in their joining. It is shown in Figure 2g that the growing tip of the pear-shaped pore pins the neighboring drop-shaped pore and hereby merges. In this joining process, several pores can be involved, which results in the formation of extended pore clusters of a complex shape. Figure 2h shows such an extended pore of volume of about 50×10^3 μm^3 and about 100 μm in length.

3. Discussion

Kirkendall porosity grows via the condensation of vacancies. Therefore, for understanding our findings, the generation, migration, and annihilation of vacancies have to be considered. Vacancies are generated and annihilated by the same structural defects such as external surface, internal surfaces (interfaces, grain boundaries, pore surfaces), and edge dislocations. If the vacancy concentration c_v is smaller than its equilibrium value c_0 (undersaturation), these defects work as sources of vacancies but if $c_v > c_0$ (supersaturation) as sinks. Whether the defects work as sources or sinks can be determined from the conservation law

$$\frac{\partial c_v}{\partial t} = -\frac{\partial J_v}{\partial z} + S \tag{1}$$

where $\partial c_v/\partial t$ is the rate of change of c_v, $\partial J_v/\partial z$ is the gradient of the vacancy flux J_v, and S a term describing the rate of generation or annihilation of vacancies. For sources, $S > 0$, and for sinks, $S < 0$. Assuming that diffusion in the diffusion couple is close to stationary and taking $\partial c_v/\partial t \approx 0$, one gets $S \approx \partial J_v/\partial z$. Thus, $\partial J_v/\partial z > 0$ indicates sources while $\partial J_v/\partial z < 0$ sinks. The same is valid for the atomic fluxes. In our previous work,[11] a change of $\partial J_v/\partial z$ across the interface CMSX-10/Ni was calculated using software Dictra. Because the nickel-base alloys are substitutional alloys, where diffusion occurs via the atom/vacancy positions exchange, it was assumed that

$$J_v = -\sum_{i=1}^{n} J_i \tag{2}$$

where J_i is the flux of the ith element and n the number of alloying elements. On the base of these modeling results, the following scenario for the evolution of Kirkendall porosity could be proposed.

Figure 3a shows a graph $\partial J_v/\partial z = f(z)$ calculated with Dictra for the end of 192 h of annealing at 1250 °C. It is predicted that in areas above $z \approx -170$ μm, the gradient of vacancy flux is positive ($\partial J_v/\partial z > 0$), which indicates vacancy sources, whereas in areas below this position, $\partial J_v/\partial z < 0$, indicating vacancy sinks. Physically, this means that during annealing a thermodynamic pump starts working which transfers vacancies top–down over the interface. Upstairs it results in a vacancy undersaturation activating the vacancy sources and downstairs in a vacancy supersaturation activating the vacancy sinks. This fits well with the experimental findings. In Figure 3b, the graph $\partial J_v/\partial z = f(z)$ is superimposed on an electron backscatter diffraction (EBSD) orientation map. Pronounced Kirkendall porosity (sinks) is observed in the areas where $\partial J_v/\partial z < 0$.

Downward from $z \approx -170$ μm, the absolute value of $\partial J_v/\partial z$ increases, reaching a sharp maximum at $z \approx -600$ μm but then lowers approaching zero; see Figure 3a. The predicted peak position is close to the border of the region where the γ′-phase is totally dissolved, extended to $z \approx -570$ μm; see Figure 1a.

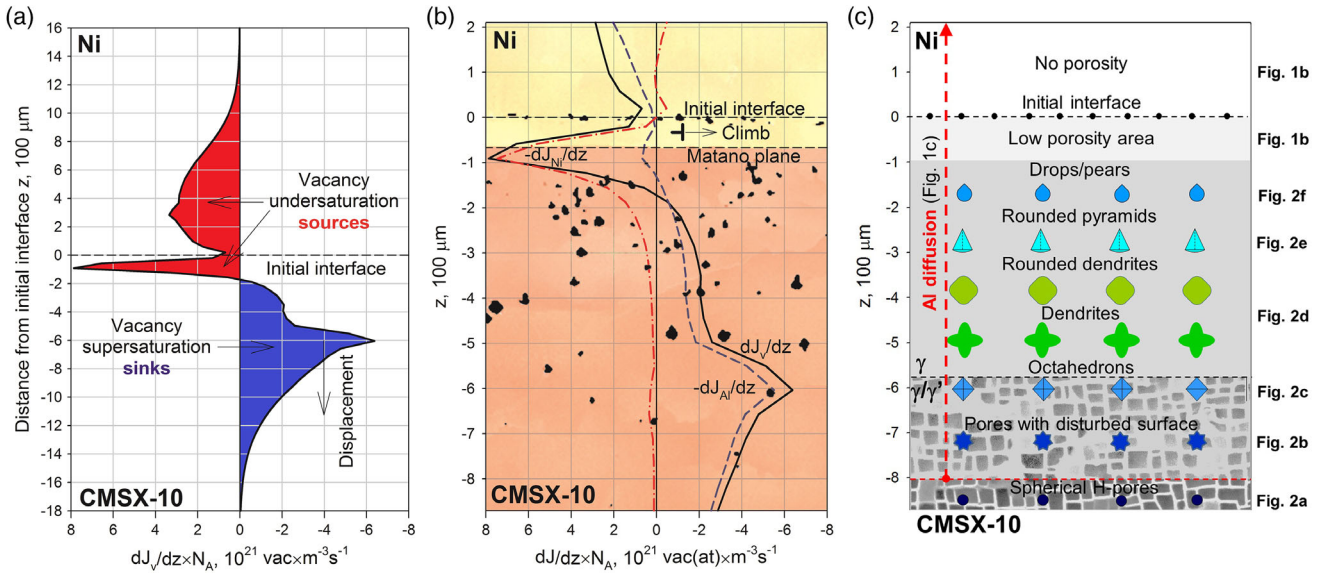

Figure 3. Gradients of diffusion fluxes and schematic of the pore shape distribution in CMSX-10/Ni couple after 192 h of annealing at 1250 °C. a) Change of $\partial J_v/\partial z$ across the interface. b) Changes of $\partial J_v/\partial z$ (black solid line), $-\partial J_{Al}/\partial z$ (blue dashed line), and $-\partial J_{Ni}/\partial z$ (red dashed–dot line). Background is an EBSD orientation map. An edge dislocation climbing between the initial and shifted interfaces is shown schematically. N_A is Avogadro constant. c) Schematic graphical summary of the porosity investigation with references to 3D images of real pores.

From the SEM image, the broader area is characterized by fast γ′-dissolution obviously working as a powerful source of Al; see a positive peak of $\partial J_{Al}/\partial z$ in Figure 3b. The released Al diffuses rapidly to Ni, activating a counterflux of vacancies according to Equation (2).

The growth rate of Kirkendall porosity depends on the absolute value of $\partial J_v/\partial z$. In the areas below the $\partial J_v/\partial z$ peak $|\partial J_v/\partial z|$ is relatively small and, therefore, the pores grow slowly. The pre-existing pores slightly increase in size taking an irregular shape (see Figure 2b) and the new octahedral pores nucleate (see Figure 2c).

At $z \approx -600$ µm, where the $\partial J_v/\partial z$ peak is located, $|\partial J_v/\partial z|$ significantly increases. This leads to the formation of protrusion in the vertices of octahedral pores changing into fast dendritic growth, see Figure 2d. Above the $\partial J_v/\partial z$ peak position $|\partial J_v/\partial z|$ again lowers. The fast dendritic growth ends and the reduction of the pore surface area now controls the evolution of pore shape. Therefore, the pores of dendritic shapes take a pear shape, see Figure 2d,f.

The rounded pyramidal pores (Figure 2e) are obviously not a result of the dendritic growth but formed due to the direct transformation of octahedral pores. Thus, in some cases, the pore development process includes an intermediate step of dendritic growth but in some cases does not. Therefore, the question arises: under which circumstances is dendritic growth realized?

Obviously, two conditions have to be satisfied for dendritic growth: first, the high rate of the local vacancy annihilation which corresponds to the $\partial J_v/\partial z$ peak and second, dwell time at the $\partial J_v/\partial z$ peak sufficient to develop dendritic arms. Thus, the most developed dendritic pores should be observed at the peak tail.

During annealing, the $\partial J_v/\partial z$ peak moves down to CMSX-10 together with the γ′ dissolution front which is located at a distance L_γ (length of γ area) from the interface. In a first approximation, one can assume that increase in L_γ is described by parabolic kinetics, i.e. $L_\gamma \approx \sqrt{D_{Al}t}$, where D_{Al} is the interdiffusion coefficient of Al in Ni and t the annealing time. Differentiating this expression by time, one gets the peak displacement velocity $v_{peak} = dL_\gamma/dt \approx \sqrt{D_{Al}/t}$, implying that during annealing the peak movement slows down. Dividing the peak width w_{peak} by v_{peak} yields the dwell time of the vacancy annihilation peak $\partial J_v/\partial z$: $t_{peak} \approx w_{peak}\sqrt{t/D_{Al}}$. Thus, during annealing, the dwell time of the $\partial J_v/\partial z$ peak increases as a function of $\sqrt{t}$, reaching maximum at the end of annealing. This is why the largest pores of dendritic shape are observed at the tail of $\partial J_v/\partial z$ peak predicted for the end of annealing. One can suggest that the development of Kirkendall pores excludes a step of dendritic growth in two cases: 1) when dwell time $t_{peak} \approx \sqrt{t}$ is too short or 2) when pores nucleate already behind the passed $\partial J_v/\partial z$ peak. Both scenarios correspond to shorter distances from the interface where rounded pyramidal- and drop-like-shaped pores are observed, see Figure 2e,f. Numerical analysis of the effect of moving $\partial J_v/\partial z$ peak on porosity growth is planned for future work.

Another feature of the graph $\partial J_v/\partial z = f(z)$ is a strong positive peak at $z \approx -70$ µm. This peak arises due to the interaction of diffusion fluxes of the alloying elements, as discussed in the study by Chyrkin et al.[11] A positive value of $\partial J_v/\partial z$ indicates that here the structural defects work as vacancy sources and not as sinks. Therefore, the area where this peak is located is nearly free of pores, see Figure 3b.

A significant finding in the study by Epishin et al.[10] was a shift of the interface visible in the EBSD orientation map (see Figure 3b) due to the migration of the high-angle boundary between the CMSX-10 crystal and the Ni grain. The [001] crystallographic axes of the CMSX-10 crystal are nearly parallel to the interface normal, whereas the [001] axis of the Ni grain deviates

by about 15° from this direction. This results in clear orientation contrast between CMSX-10 and Ni in the EBSD map. Because the area located between the original and shifted interfaces has the same crystallographic orientation as the nickel grain, this shift can be interpreted as the growth of the Ni grain toward CMSX-10. It is remarkable that the position of the interface that shifted down by about 70 μm coincides with the position of Matano plane shown by a dashed horizontal line in Figure 3b. This interface shift can be explained considering a graph $\partial J_{Ni}/\partial z = f(z)$ for the base element Ni which gives the main contribution to the positive $\partial J_v/\partial z$ peak, see Figure 3b. $\partial J_{Ni}/\partial z < 0$ indicates the sink of Ni atoms arriving from the Ni part. These atoms can condense directly on the migrating interface or on the half extra-planes of edge dislocations climbing, as schematically shown in Figure 3b. Both processes result in the interface shift toward CMSX-10.

Figure 3c shows a graphical summary of the porosity investigation. Here the main types of observed pores and their locations are schematically shown. The distribution of the pore shapes can be compared with the shape of simulated profiles of the gradient of diffusion fluxes shown in Figure 3b. On the right side of Figure 3c, references to figures with 3D images of real pores are given.

4. Conclusions

1) Kirkendall porosity that formed during interdiffusion in a diffusion couple CMSX-10/Ni at 1250 °C was investigated using X-ray sub-μ tomography. It was found that at this temperature the pores nucleate as {111}-faced octahedrons, but the subsequent evolution of their shape can be different. Two sequences of the evolution of the pore shape are assumed depending on the distance from the interface; closer to the interface: octahedrons → rounded pyramid → drop shape, and far from interface: octahedrons → dendrites → pear shape. Near the interface, the grow rate of Kirkendall pores becomes anisotropic and maximal in the direction to the vacancy source. The directed growth of pores results in their coalescence. 2) The experimental findings are explained on the basis of results of interdiffusion modeling using Dictra considering the two-phase γ/γ′ microstructure of superalloy CMSX-10. It is shown that fast dendritic pore growth occurs at the front of γ′ dissolution where the local rate of vacancy annihilation, characterized by $\partial J_{Al}/\partial z$, has a maximum. Closer to the interface, the magnitude of $\partial J_{Al}/\partial z$ is lower, the pore growth slows down, and the pores round out under the surface tension taking a rounded shape. 3) The interface displacement visible in the EBSD orientation map as growth of the Ni grain toward CMSX-10 results from the sink of Ni atoms coming from the Ni part. This is indicated by the negative $\partial J_{Ni}/\partial z$ peak resulting from the interaction of diffusion fluxes of alloying elements as described in the study by Chyrkin et al.[11]

5. Experimental Section

The diffusion couple under investigation was assembled from a [001] single crystal of nickel-base superalloy CMSX-10 and a polycrystal sample of high-purity nickel. Superalloy CMSX-10 was developed by the Cannon Muskegon Corporation, USA.[19] Its chemical composition is characterized by high concentrations of refractory elements. In particular, this alloy contains 6 wt.% rhenium and, according to the accepted classification, belongs to the third generation of single-crystal superalloys. The used [001] single crystal of CMSX-10 was solidified and fully heat treated by Doncasters Precision Castings, Bochum, Germany. The nickel sample was produced by zone melting. It had a columnar grain structure with a transverse grain size of a few millimeters. The initial porosity in fully heat-treated CMSX-10 was (0.3 ± 0.045) vol% as measured by synchrotron tomography in our previous work[9]; the initial porosity of the nickel sample was close to zero.

The CMSX-10 and nickel bars were cross cut into 2.5 mm-thick disks of diameter 12 mm. Both sides of the disks were ground. Subsequently, the joining sides were polished using diamond pastes, finished with a particle size of 1 μm. The polished surfaces of the disks were joined by 1 h of diffusion welding in a MTS-810 testing machine using induction heating under vacuum of about 10^{-6} mbar at a temperature of 1050 °C and a compressive stress of 10 MPa. The diffusion couple was sealed in an ampoule of fused quartz under vacuum of about 10^{-6} mbar and annealed at 1250 °C for 192 h. After annealing, it was investigated by SEM and EPMA as reported in a study by Epishin et al.[10] and then used for tomographic investigations in this work.

For synchrotron tomography, two cylindrical samples were cut by spark erosion from the diffusion couple perpendicular to the interface. The samples had a diameter of 1 mm and a length of 10 mm. Tomography experiments were conducted at the beamline ID19 at the ESRF in Grenoble, France. A monochromatic beam with an energy of 70 keV and a current of 200 mA (7/8 multibunch mode) was used. The radiographs were recorded in absorption contrast with a sCMOS camera PCO EDGE 4.2 with a resolution of 2048 × 2048 pixel. The continuous 360° rotation of the sample stage enabled an effective measuring field of 3700 × 3700 × 2048 voxel with a spatial image size of 1265 × 1265 × 700 μm^3. This corresponded to a voxel size of 0.347 μm^3 in the reconstructed tomograms. During one complete rotation of the sample stage, about 5000 radiographs were recorded with an exposure time of 50 ms/radiograph. Thus, a total measuring time was about 5 min per tomogram. The evaluation of the tomograms was done with the defect analysis tool of the commercial visualization software VGStudioMax (Version 2.1) of the company Volume Graphics.

Acknowledgements

The authors acknowledge the European Synchrotron Radiation Facility for provision of synchrotron radiation facilities and the authors would like to thank Mrs. Elodie Boller and Mr. Jonas Schmidt for assistance in using beamline ID19. This work was supported by the German Research Foundation, project EP 136/1-1. Open Access funding enabled and organized by Projekt DEAL.

Conflict of Interest

The authors declare no conflict of interest.

Keywords

diffusions, nickel alloys, porous materials, synchrotron radiations, three-dimensional tomographies

Received: October 14, 2020
Revised: November 30, 2020
Published online:

[1] F. Seitz, *Acta Metall.* **1953**, *1*, 355.
[2] F. Aldinger, *Acta Metall.* **1974**, *22*, 923.
[3] K. Garbala, A. Patejuk, *Arch. Foundry Eng.* **2010**, *10*, 455.

[4] A. M. Gusak, N. V. Storozhuk, *Phys. Met. Metallogr.* **2013**, *114*, 197.
[5] A. Gusak, B. Wierzba, M. Danielewski, *Pholos. Mag.* **2014**, *94*, 1153.
[6] B. Wierzba, *Phys. A* **2014**, *403*, 29.
[7] B. Wierzba, *Phys. A* **2014**, *413*, 71.
[8] J. Svoboda, F. D. Fischer, *Comput. Mater. Sci.* **2017**, *127*, 136.
[9] T. Link, S. Zabler, A. Epishin, A. Haibel, M. Bansal, X. Thibault, *Mater. Sci. Eng. A* **2006**, *425*, 47.
[10] A. Epishin, T. Link, G. Nolze, I. L. Svetlov, B. S. Bokstein, A. O. Rodin, R. Saliwan Neumann, G. Oder, *Phys. Met. Metallogr.* **2014**, *115*, 21.
[11] A. Chyrkin, A. Epishin, R. Pillai, T. Link, G. Nolze, W. J. Quadakkers, *J. Phase Equilib. Diff.* **2016**, *37*, 211.
[12] H. Leszczyński, K. Lademan, K. Tkacz-Śmiech, B. Bożek, M. Zajusz, M. Danielewski, *Nano Hybrids Compos.* **2019**, *26*, 20.
[13] A. Epishin, T. Link, U. Brückner, P. D. Portella, in *Proc. 7th Liège Conf. Materials for Advanced Power Engineering* (Eds: J. Lecomte-Beckers, M. Carton, F. Schubert, P. J. Ennis), FZ Jülich, Jülich **2002**.
[14] A. Epishin, T. Link, I. L. Svetlov, G. Nolze, R. Salivan Neuman, H. Lucas, *Int. J. Mater. Res.* **2013**, *104*, 776.
[15] J. Lecomte-Beckers, *Metall. Trans. A* **1988**, *19*, 2341.
[16] S. G. Wang, E. K. Tian, C. W. Lung, *J. Phys. Chem. Solids* **2000**, *61*, 1295.
[17] Y. N. Wen, J. M. Zhang, *Solid State Commun.* **2007**, *144*, 163.
[18] R. I. Garber, V. S. Kogan, L. M. Poliakov, *Sov. Phys. JETP* **1959**, *35*, 953.
[19] G. L. Erickson, *JOM* **1995**, *47*, 36.